Bragg scattering and Brownian motion dynamics in optically induced crystals of submicron particles

R. E. Sapiro, B. N. Slama, and G. Raithel

Phys. Rev. E **87**, 052311 — Published 29 May 2013

DOI: 10.1103/PhysRevE.87.052311

Bragg scattering and Brownian motion dynamics in optically induced crystals of sub-micron particles

R. E. Sapiro, B. N. Slama, and G. Raithel
Department of Physics, University of Michigan, Ann Arbor, MI 48109

A set of four confocal laser beams of 1064 nm wavelength is used to prepare optically induced crystals of sub-micron particles in aqueous solution. Thousands of polystyrene spheres of about 200 nm diameter are trapped in three dimensions. Bragg scattering patterns obtained with a probe beam of 532 nm wavelength are in agreement with the calculated lattice structure and its polarization dependence. The decay and rise of the Bragg scattering intensity upon switching the lattice off and on reveals the Brownian motion dynamics of the particles in the periodic optical trapping potential. Experimental results agree well with results from trajectory simulations based on the Langevin equation. The results exhibit the interplay between Brownian motion and deterministic forces in an inhomogeneous (near-)periodic optical trapping potential.

PACS numbers: 83.80.Hj,42.50.Wk,83.10.Mj,83.10.Rs

I. INTRODUCTION

Optical traps for particles in solution (optical tweezers), pioneered by Ashkin in the 1970's and 80's [1–3], are now used in a variety of applications [4, 5]. There has been rising interest in trapping geometries with multiple trapping sites, allowing for the preparation and manipulation of many particles at the same time. Techniques include interference of multiple laser beams within the trapping volume [6–10], as well as holographic techniques that generate multiple static or dynamic trapping sites [11–15]. Generally, several issues need to be addressed in these setups. First, the trapping of multiple particles typically requires an equilibrium of the radiation pressure forces acting on the particles [4, 16, 17]. Sometimes auxiliary normal forces from sample cell boundaries are used. In the present work, we employ a radiation-pressure-balanced optical lattice formed by four 1064 nm laser beams that intersect at a confocal point [18]. The optical lattice generates a three-dimensional (3D) array of periodic traps for sub-micron polystyrene spheres (refractive index $n_{\rm p} = 1.59$, diameter ~ 200 nm). Second, multi-site traps require higher laser power than single-trap tweezers since the light energy present within the trapping volume scales with the number of trapping sites. Thus, traps with many sites are susceptible to unwanted heating and convection. Our laser trapping geometry, which is akin to setups that have been used in atom trapping [19, 20], exhibits a high volume density of trapping sites such that the light power required per site is fairly small (of order only 1 mW). Several thousand particles can be trapped before heating causes noticeable effects.

We employ Bragg scattering of green laser light to verify the crystal structure and its dependence on laser polarization. Because of the dependence of the Bragg scattering signals on the Deybe-Waller factor, the Bragg scattering data allow us to study the thermal spread of the particles about their ideal trapping sites. Our results set the stage for trapping and Bragg structure analysis of non-trivial particles (viruses, large bio-molecules, etc.) using shorter-wavelength radiation. This potential application represents one motivation for our work. The optical crystals under investigation are mostly defect-free, exhibiting a near-100% occupation probability of lattice sites. Neighboring trapped particles are in close proximity of each other (distances a few hundred nm), forming densely packed optical crystals. A large volume filling fraction, available with larger particles, is conducive to the preparation of tuneable photonic bandgap media, waveguides, optical resonators and other nano-fabricated optical structures. This prospect represents a second motivation for the work. In densely packed optical crystals one may expect particle interaction effects as well as back action between the optical fields and the particle system. Light-induced particle interactions can produce regular structures ("optical matter"; see, *e. g.*, Ref. [6]). In the present paper, in one of the polarization cases discussed it appears that the combination of a 2D optical lattice potential and particle-particle interactions can lead to a 3D crystal (Sec. VI D).

Direct visual observation of the crystal formation [18] indicates that the crystallization dynamics as well as the degree of particle localization are driven by the competition between Brownian motion and the forces induced by the optical trapping potentials. A quantitative understanding of Brownian motion effects represents an important prerequisite to applications of optically induced crystals of sub-micron particles in solution. Here, we use Bragg scattering to study the Brownian motion dynamics in such a system. To explain the results, we numerically solve the Langevin equation for particle ensembles [21]. The derived simulated Bragg scattering signals agree well with experimental data.

II. PHYSICAL CONCEPTS

We first provide an overview of important concepts that apply to our experimental system. Optical forces on polystyrene particles in aqueous solution are gener-

ated by four intersecting, mutually-coherent laser beams that generate a 3D interference pattern, a method we presented in Ref. [18]. The optical setup is sketched in Fig. 1. Under the influence of the optical forces, the polystyrene particles lock into place at the light interference maxima, which are located on a periodic grid. The optical-crystal period scales with the wavelength of the lattice light and the beam geometry. In our case it is on the order of 500 nm in all three directions. The crystals fill volumes of about $(5\ \mu\text{m})^3$. The trapping sites typically have a depth between 10 and 100 k_BT at a temperature $T \approx 300$ K. Geometrically, only one particle can fit within a site. After several minutes of the lattice beams being on, in the central region of the lattice where the wells are deeper than several k_BT, all wells become filled with near-unity probability, with exactly one trapped particle per well. The water solvent provides a Stokes friction force, due to which the particles lose energy, while the optical forces pull the particles into the wells. The water solvent also adds Brownian motion. Situations of this nature are treated in textbooks (see, for instance, Ref. [21]).

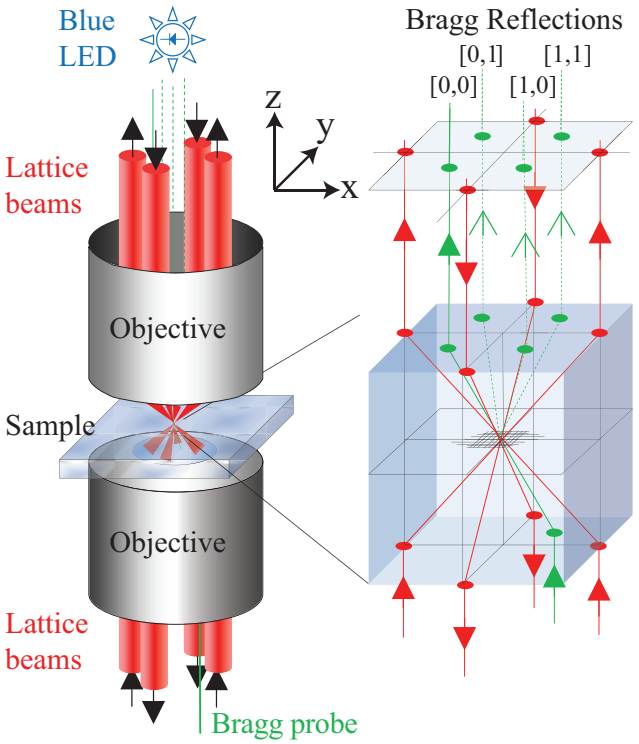

FIG. 1. Schematic of the experimental setup. (Color online.)

The particle dynamics follow from the interplay between the random force that causes the Brownian motion, friction, and the position-dependent, periodic, conservative optical-trapping force. The resultant motion has several characteristic time scales. The time interval between random collisions between the particles and the water molecules, on the order of 10^{-18} s, is much too short to be observable. The velocity correlation time, or damping time associated with the Stokes friction force, is ≈ 5 ns and is also too short to be observable in our experiment. Brownian motion and its associated diffusion manifest as the particles hopping from place to place from one image frame to the next. This is typical in experiments with limited time resolution (such as ours). The time particles need to diffuse over one lattice-laser wavelength, *i. e.* the characteristic length scale of the setup, is on the order of 50 ms. When the lattice is turned on, the particles that are already within the lattice volume drift into the nearest well within a time on the order of 1 ms, due to the combined effects of the optical force and the retardation caused by the Stokes friction force. This optically-driven particle drift into the wells is slow enough that we are able to observe it in real time. The time it takes for an entire crystal to form "from scratch" is governed by the rate at which faraway particles diffuse into the lattice region, which is dependent on the particle concentration. The crystal formation time typically is several minutes.

The oscillation period of the particles in the optical-lattice wells in absence of damping (*i.e.* in absence of any water molecules, in vacuum) would only be on the order of 10 μs. In water, the motion of the particles in the optical-lattice wells is heavily over-damped. Since the wells are quite deep compared to k_BT, the particles settle in the lattice wells and follow a Maxwell-Boltzmann phase-space distribution. In steady-state, the spread of the particles from the lattice-well minima corresponds to an average potential energy of the particles in the optical trapping potential of $(3/2)k_BT$ above the bottoms of the wells. Hence, the root-mean-square displacement of the particles from the centers of the lattice wells, caused by random Brownian-motion-style excursions, scales with the inverse square root of the well depth, which is proportional to the lattice-laser power. By increasing the laser power the particles become better localized in the wells. This effect is clearly visible in the experiment. At high laser power the Brownian motion appears to practically "freeze out" and the particles appear locked into fixed positions. We can also intentionally induce changes in the optical force by changing the lattice depth. The ensuing drift motion reflects the particles' response to changes in the optical force, as well as the Stokes friction force which acts while the particles are drifting. The ubiquitous random force adds the Brownian, random component to the motion.

We use Bragg scattering to analyze the static and dynamic properties of the optically induced crystals. Our Bragg probe wavelength is $\gtrsim 3$ orders of magnitude longer than those used in x-ray Bragg scattering from solid-state crystals, and the spatial periods of the optically induced crystals are ~ 3 orders of magnitude larger than those in solid-state crystals.

III. SETUP

The 3D optical lattice is generated using four beams derived from a single laser (air wavelength $\lambda_0 = 1064$ nm, line-width < 1 MHz) similar to the setup described in [18]. As illustrated in Fig. 1, the four beams are grouped into a down-going pair and an up-going pair of parallel beams. The down-going (up-going) pair of beams is separated by 4.2 mm on the y- (x-)axis; the two pairs enter through identical microscope objectives (Nikon 100x, 1.25 N.A., oil immersion, ∞-corrected). The transmission of the objectives at 1064 nm is about 60%. The microscope objectives are aligned along a shared optical axis to a common confocal point. The gap between the objectives is 0.41 mm (the sum of the manufacturer's specification for the working distances). A sample cell is placed between the two objectives, with oil filling the small volumes between the objectives and the cell surfaces. Sample cells are made from two 150 μm thick microscope cover slips fused together with $\lesssim 100$ μm thick strips of paraffin film. The cell volume is about 1 cm^2 $\times \lesssim 100$ μm, with clear optical access through the 1 cm^2 top and bottom surfaces. The cells are filled with an aqueous solution of spherical polystyrene particles at a concentration of about 10^9 particles/cm^3, with 0.05% v/w Tween 20 to prevent aggregation. In the present work, particle diameters are 190 nm or 250 nm. Prior to turning the lattice on, the particles are randomly distributed, with a practically constant average density. The vertical position of the sample cell is adjusted such that the confocal point and the optically induced crystals are located within the bulk of the solution, away from all glass surfaces.

All four optical-lattice beams enter the microscope objectives parallel to the z-axis, at distances of 2.1 mm away from the optical axis, as shown in Fig. 1. As they pass through the objectives, they are refracted towards the confocal point, where they pass through the common focal spot. The four propagation vectors within the sample volume are $k(\pm\sin(\phi), 0, \cos(\phi))$ and $k(0, \pm\sin(\phi), -\cos(\phi))$. The beams have identical angles ϕ relative to the optical axis of the microscope objectives and wavenumber $k = 2\pi n_{\rm w}/\lambda_0$ (the refractive index of water $n_{\rm w} = 1.33$). This beam configuration forms a 3D optical lattice using a minimal number of beams [22, 23]. We have experimentally determined $\phi = 52^o \pm 2^o$ in pure water. Taking into account the small refractive index change due to the particles, we estimate $\phi = 50^o \pm 2^o$ inside the lattices. The resulting trapping potentials are close to those explicitly provided in Ref. [18] for the case $\phi = 45^o$. With the lattice turned off, diffusion is by far the dominant source of motion and gravity is negligible (it takes the particles about one day to accumulate near the bottom of the cell). With the lattice turned on, Brownian motion and conservative light forces are in competition with each other, and gravity plays even less of a role than with the lattice off.

Two real-time detection methods are employed to examine the optical crystals. The first is direct spatial imaging, using a blue LED (center vacuum wavelength 450 nm) to illuminate the optical lattice. The LED is focused into the back aperture of the top microscope objective, which acts as a collimator. The blue light scattered from the sample is collected by the bottom objective, where it is split off by a dichroic mirror and imaged onto a CCD camera. The camera is mounted on a translation stage, allowing the imaging plane to be adjusted over several microns to observe different planes of the lattice along the z-axis. The second detection method is Bragg scattering. This method has previously been used to study the localization and the wave-packet dynamics of laser-cooled atoms in optical lattices [24–28]. As shown in Fig. 1, a green Bragg probe laser beam (vacuum wavelength 532 nm, diameter ~ 0.5 mm) enters the bottom microscope objective parallel to the lattice beams and is focused onto the optical crystal. This wavelength is longer than the diameter of the polystyrene spheres (190-250 nm), so for our present level of precision they can be approximated as point particles. The location and angle of the probe beam relative to the lattice beams near the back aperture of the microscope lens is chosen such that several Bragg reflections can be observed simultaneously. In the case illustrated in Fig. 1, the lattice beams form an angle of $\phi \approx 45^o$ relative to the z-axis, while the Bragg probe and all three visible Bragg-reflected beams form angles of $\approx 30^o$ relative to the z-axis (beam positions and angles are approximately to scale in the figure). The Bragg probe beam and its forward Bragg reflections exit through the top microscope objective, where they are split off from the lattice beams by a dichroic mirror. They are projected onto a paper screen imaged by a camera. A photodiode can be placed in the path of any of the Bragg-scattered beams to measure the Bragg intensities as a function of time.

In accordance with the potentials provided in section III.A of Ref. [18], we find that the lattice beam polarizations have a profound effect on the images and on the Bragg scattering behavior of the particle crystals. We denote a beam pair as p-polarized if its polarization is linear and in the plane spanned by that beam pair, and as s-polarized if its polarization is linear and transverse to that plane. To specify the polarizations of both beam pairs, we list the polarization of the down-going pair first (*e.g.*, *sp*-polarization denotes s-polarization of the down-going pair and p-polarization of the up-going pair).

IV. LATTICE STRUCTURE AND BRAGG SCATTERING GEOMETRY

The value of ϕ is sufficiently close to 45° that we perform all calculations for $\phi = 45°$. For the cases of *pp*-, *sp*-, and *ps*- polarization, the lattice potential has an apparent face-centered orthorhombic (FCO) structure with a tetragonal unit cell of lengths $a = b = \sqrt{2}\lambda$ and $c = \lambda/\sqrt{2}$ along the x, y and z-directions, respectively

(see Fig. 2(a)). There, λ is the effective wavelength of the lattice laser in the water-particle mix in the lattice, $\lambda \approx 1064$ nm/1.35. The potentials are given in Ref. [18]. The primitive unit cell of this lattice is monoclinic, and its unit vectors can be written in Cartesian coordinates as $\mathbf{a}_1 = (a/2, -a/2, 0)$, $\mathbf{a}_2 = (a/2, a/2, 0)$ and $\mathbf{a}_3 = (a/2, 0, c/2)$. The corresponding reciprocal lattice has unit vectors $\mathbf{k}_1 = 2\pi(1/a, -1/a, -1/c)$, $\mathbf{k}_2 = 2\pi(-1/a, -1/a, 1/c)$ and $\mathbf{k}_3 = 2\pi(0, 0, 2/c)$. Our current setup does not allow observation of Bragg scattering orders with non-zero z-components of the reciprocal lattice vectors $\Delta\mathbf{k} = h\mathbf{k}_1 + k\mathbf{k}_2 + l\mathbf{k}_3$. Thus, we only observe Bragg peaks from planes with Miller indices (hkl) that satisfy $2l + k - h = 0$, leading to

$$\Delta\mathbf{k} = \frac{4\pi}{a}(n_x, n_y, 0) = \frac{2\sqrt{2}\pi}{\lambda}(n_x, n_y, 0) \qquad (1)$$

with integers $n_x = l$ and $n_y = l - h$. For simplicity we denote the observed reflections $(n_x n_y)$. As shown in Figs. 1 and 2(c), we choose a Bragg probe beam alignment that allows us to simultaneously analyze the Bragg reflections (10), (01) and (11); the probe beam itself is denoted (00). Bragg orders higher than $n_i = 1$ are not presently observed. The probe beam and the (10), (01) and (11) Bragg reflections all form angles of $\approx 30°$ relative to the z-axis. As indicated in Fig. 1, in the back plane of the microscope objectives the probe beam and the (10), (01) and (11) Bragg reflections form a square that is oriented at 45° relative to the square formed by the four lattice beams. Forward Bragg scattering with $\Delta k_z = 0$ does not provide information about the crystal structure or the particle spread from the ideal sites in the z degree of freedom.

In the case of *ss*-polarization, the light-induced trapping potential is periodic in x and y, but not in z (see Ref. [18] Eq. 1 and Fig. 2(b)). The resultant two-dimensional (2D) lattice has elementary unit vectors $\mathbf{a}_1 = (a/2, 0)$ and $\mathbf{a}_2 = (0, a/2)$, and the reciprocal lattice has unit vectors $\mathbf{k}_1 = 4\pi(1/a, 0)$ and $\mathbf{k}_2 = 4\pi(0, 1/a)$, leading to the same $\Delta\mathbf{k}$ as in Eq. 1. Since we only observe Bragg scattering with $\Delta k_z = 0$, we expect and observe that all four polarization cases yield the same Bragg scattering peaks, with intensities depending on polarization.

We define the reflectivity for the Bragg peak $(n_x n_y)$ as $R_{n_x n_y} = P_{n_x n_y}/P_0$, where P_0 is the incident Bragg probe power and $P_{n_x n_y}$ is the power reflected into peak $(n_x n_y)$. In lattices that are symmetric under x-y swap, we expect $R_{10} = R_{01}$. In a homogeneous crystal and in the case of low saturation, *i.e.* if all $R_{n_x n_y} \ll 1$, the Bragg reflectivities are proportional to the respective Debye-Waller factors, $R_{n_x n_y} = cD_{n_x n_y}$, where the proportionality constant c should be the same for all Bragg reflections. The constant c is related to the number of particles, the overall shape of the crystal, the crystal's position within the probe beam, etc. The Debye-Waller factor is

$$D = \exp\left(-\left\langle(\Delta\mathbf{k}\cdot\Delta\mathbf{x})^2\right\rangle\right) \quad ,$$

where $\hbar\Delta\mathbf{k}$ is the photon momentum exchange from Eq. 1

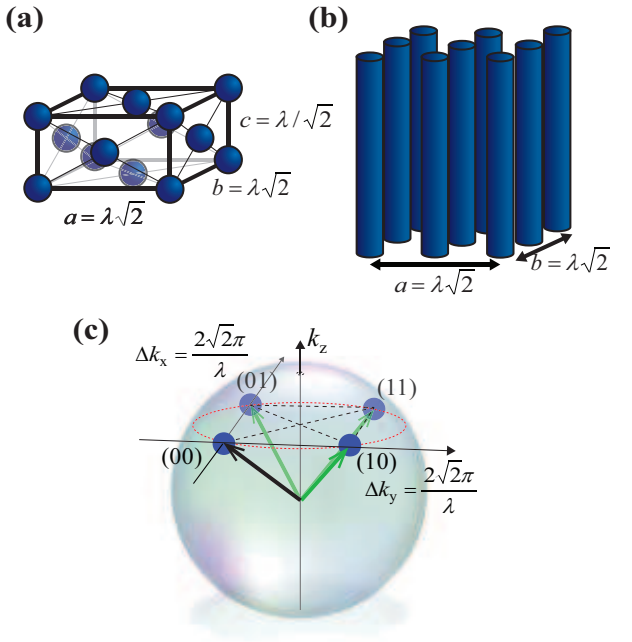

FIG. 2. (a) Apparent face-centered orthorhombic lattice structure for *pp*-, *sp*- and *ps*-polarizations. (b) The lattice potential structure for *ss*-polarization is constant in z. (c) Ewald sphere (radius= $2\pi/\lambda_{probe}$) for the utilized Bragg scattering geometry with $\Delta k_z = 0$. (Color online.)

associated with individual Bragg reflections, and $\langle ... \rangle$ indicates an average over all particles in the crystal. The vector $\Delta\mathbf{x}$ is the displacement of a particle from its ideal crystal site. In the present case, the deviations $\Delta\mathbf{x}$ are caused by Brownian motion in the trapping potential wells. We refer to the root-mean-square deviation of the particles from their sites as *localization*: x-localization is $\sqrt{\langle\Delta x^2\rangle}$, etc.

For $\phi = 45°$, the Debye-Waller factors for the (10), (01) and (11) reflections are:

$$\begin{aligned} D_{10} &= \exp\left(-\kappa^2(\Delta\mathrm{x})^2\right) \\ D_{01} &= \exp\left(-\kappa^2(\Delta\mathrm{y})^2\right) \\ D_{11} &= \exp\left(-\kappa^2\left[(\Delta\mathrm{x})^2 + (\Delta\mathrm{y})^2\right]\right) \quad , \end{aligned} \qquad (2)$$

where $\kappa = 2\sqrt{2}\pi/\lambda$. Note that $D_{11} = D_{01}D_{10}$. If the trapping potential is invariant under x-y swap, $D_{01} = D_{10}$ and $D_{11} = D_{01}^2$. Several useful relations apply that allow, in principle, calculation of the particle localizations in x and y from measured ratios of Bragg reflectivities:

$$\begin{aligned} D_{01} &= \frac{R_{11}}{R_{10}} \\ D_{10} &= \frac{R_{11}}{R_{01}} \\ D_{11} &= \frac{R_{11}}{R_{10}}\frac{R_{11}}{R_{01}} \end{aligned} \qquad (3)$$

V. STRUCTURE AND BRAGG SCATTERING OF LARGE CRYSTALS

In Fig. 3(a), we show an optically induced crystal of 250 nm diameter polystyrene spheres generated by the four-beam optical lattice with *ss*-polarization. The total laser power is 3 W (summed over all lattice beams and measured before the microscope objectives). The crystal is prepared in the bulk of the sample, away from all walls, and contains several thousand particles. The crystal is 10-15 sites wide on each of the x- and y-axes; additionally, it is many lattice sites deep along the z-axis. The volume of the crystal is controlled by the beam waists, the angle ϕ, and the intensity of the lattice beams. The fine adjustment of the positions of the focal spots of the laser beams relative to each other also plays a role. The beam waist, or size of the focal spots, directly determines how wide the lattice will be. It can be adjusted by changing the diameter of the lattice beams before they enter the microscope objectives (a smaller initial diameter leads to a larger-diameter focal spot). Here, the diameter is 0.5 mm, leading to beam waists at the confocal point of about 5 μm diameter. The incident angle of the beams determines the lattice period, with larger ϕ leading to smaller periods in the x- and y-directions and longer periods in the z-direction. The angle ϕ is determined by the spacing between the parallel lattice beams, which is 4.2 mm in the current setup, leading to $\phi = 50^o \pm 2^o$. The most straightforward way to control the lattice volume and the particle localization is to vary the lattice laser power. As the lattice power increases, the lattice becomes deep enough to trap particles farther out from the center, thus increasing the volume of the optical crystal. In our experiments, we use laser powers ranging from 0.5 W to 4 W split evenly among the four lattice beams, amounting to central beam intensities ranging up to about 2×10^{10} W/cm^2 per beam.

The crystal shown in Fig. 3(a) took several minutes to form after turning on the laser (the laser is immediately switched on to full power). Initially there are almost no particles in the optical trapping region, as the particle density in the solution outside the lattice is three to four orders of magnitude lower than the density of lattice sites. Thus, particles need time to diffuse into the optical trapping region. As the trapping volume fills up, particles are typically first caught in the periphery of the growing crystal, and then jump from potential well to potential well to fill the innermost, deepest wells (see Ref. [18] Fig. 3(a),(b)). As the crystal nears its steady-state configuration, all lattice sites with a minimal depth of several k_BT become occupied. Thus, in steady-state all sites within the center region of the optically-induced crystals are filled; vacancies only occur on the surface. With good optical alignment, crystals are formed with a well-defined perimeter of circular to diamond shape. Approximate overall radiation pressure equilibrium is essential for obtaining large crystals; misalignment leads to particle escape along the direction(s) of dominant radiation pressure.

Considering the large refractive index gradient between water and polystyrene (1.33 vs 1.59), it is remarkable that stable optically-induced crystals with more than ten lattice planes can form at all. Stable crystals that exhibit near-perfect symmetry require all four laser beams to be present at all locations throughout the crystal volume. Notably, for locations near the surface of the crystal, this includes beams that propagate all the way through the crystal before reaching those locations. In view of the large refractive index gradient between particles and solvent, we believe that the observed large optically induced crystals are only possible because the particle system and the light fields reach a self-consistent equilibrium state. Similar situations have been discussed, within a cold-atom context, in Ref. [29]. The likely self-consistent equilibrium state has two components. First, the light-induced forces on all particles must cancel to result in a stable crystal. Second, we note that the reciprocal lattice vectors, given in Sec. IV, are identical with differences of wave-vectors of pairs of optical-lattice beams. The optically-induced crystal can thus Bragg-diffract power out of any of the four optical-lattice beams into the others. Therefore, in the likely equilibrium state, the four lattice beams must exhibit no net gain or loss due to Bragg diffraction as they propagate through the crystal.

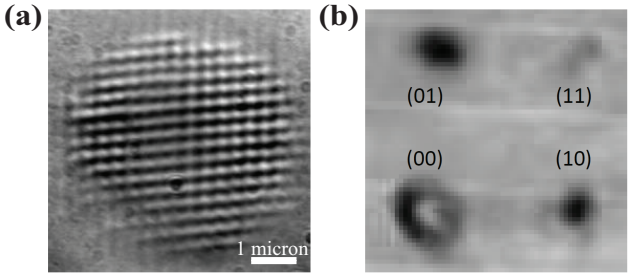

FIG. 3. (a) CCD image of a large optically induced crystal with thousands of 250 nm diameter particles (3 W total power, *ss*-polarization). (b) Bragg scattering pattern of the crystal with Bragg peak assignments as in Fig. 2.

Figure 3(b) shows the Bragg scattering pattern from the crystal in Fig. 3(a), obtained with the 523 nm Bragg probe beam depicted in Fig. 1. The positions of the Bragg peaks in the detection plane match our expectations described in Sec. IV. The (11) peak is considerably weaker than the (01) and (10) peaks. This is expected because the momentum transfer of the (11) peak is a factor of $\sqrt{2}$ larger than that of the (01) and (10) peaks. The pattern in Fig. 3(b) is saturated: the Bragg peaks have about the same intensity as the non-diffracted peak. The non-diffracted peak has a "shadow" at its center, because most of the incident light is Bragg-scattered out of the central region of the Bragg probe beam.

The shadow seen in Fig. 3(b) makes it clear that in large crystals the Bragg probe light does not penetrate deeply into the crystal. Much of the Bragg scattering

occurs on the surface, where the lattice beam intensities are low and the particles are less strongly localized than at the center. Therefore, while images such as the ones in Fig. 3(b) nicely demonstrate the Bragg scattering of optically induced crystals, less-saturated Bragg scattering is necessary for quantitative studies. To avoid saturation and multiple scattering effects, and to ensure that Bragg probe light reaches the crystal center, the measurements discussed in Sec. VI are performed with smaller particles (190 nm diameter), which scatter much less green light. In the time-dependent measurements in Secs. VII and VIII, saturation is avoided by using less trap-laser power, creating smaller crystals. In the unsaturated limit, the fields and powers of the Bragg-reflected beams are expected to scale as the particle number and the square of the particle number, respectively.

VI. POLARIZATION DEPENDENCE OF BRAGG SCATTERING

A. PP-polarization

For the case of negligible particle-particle interactions, trapping potentials have previously been given in Ref. [18]. Under the assumptions that the particles exhibit an isotropic, polarization-independent response to the light field and that the back-action of the trapped particles onto the field can be neglected, the trapping potential is [30]

$$W(\mathbf{x}) = -\frac{3(n_{\rm p}^2 - n_{\rm w}^2)}{2c(n_{\rm p}^2 + 2n_{\rm w}^2)} \int_{\text{particle volume}} I(\mathbf{x}')dx'\,dy'\,dz' \quad , \tag{4}$$

where the integral is over the single-particle volume and $I(\mathbf{x}')$ is the field intensity (which depends on beam directions and polarizations). For 190 nm diameter particles, the volume filling fraction in the FCO structure shown in Fig. 2 is only 2 % [18]. Therefore, the interaction-free optical trapping potentials of Eq. 4 are expected to be fairly accurate. In this Section, we show that the relative strengths of Bragg scattering peaks follow qualitative predictions based on the trapping potentials $W(\mathbf{x})$.

We note that polarization gradients, which are inherent to the lattice fields used in our present work [23, 31], do not enter into Eq. 4 due to the assumption of an isotropic response of the particles. This is in stark contrast to laser cooling and trapping of atoms (from which this technique derives), where the non-isotropic spin structure of the atoms can enable laser cooling methods that do depend on the presence of polarization gradients ("Sisyphus cooling"; see [32] and references therein).

In Fig. 4 we show a CCD image (top left) and Bragg scattering pattern (top right) of a crystal of 190 nm particles, induced with a laser power of 3 W and *pp*-polarization. The bottom part of Fig. 4 shows several cuts through the corresponding trapping potential. The

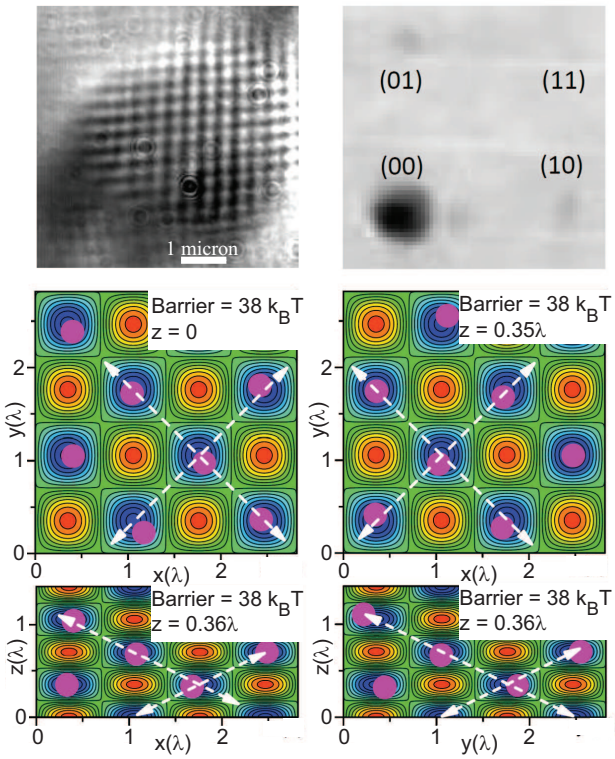

FIG. 4. Top: image (left) and Bragg scattering pattern (right) with total laser power 3 W, *pp*-polarization, and 190 nm diameter particles. The gray scale for the Bragg image shows the square root of intensity, to emphasize small signals. Bottom: cuts through the trapping potential calculated for $\phi = 45°$ and an intensity of 2×10^{10} W/m^2. The color scale ranges from -80k_BT (blue) to 0 (red) in steps of 5k_BT. The indicated barrier heights correspond to particle diffusion along the paths indicated by the white arrows. The pink dots indicate the size of the particles. (Color online.)

images are taken after allowing the crystals several minutes to reach steady-state. The image, the Bragg pattern, and the potential are symmetric under swapping of x and y. The potential cuts reflect the FCO lattice structure with periods $a = b = \sqrt{2}\lambda$ and $c = \lambda/\sqrt{2}$ along the x, y and z-directions. The Bragg peaks (10) and (01) are equally intense and clearly visible, while there only is a faint hint of a (11) peak. To interpret this behavior, we note that, for cases symmetric under $x - y$ swap and for homogeneous crystals, the Debye-Waller factor for peak (11) should equal the product of that of the (10) and (01) peaks (see Eq. 2). Thus, with the (10) and (01) peaks fairly dim in Fig. 4, it is reasonable for the (11) peak to be very weak. The values for the potential barriers given in Fig. 4 are for a single-beam intensity of 2×10^{10} W/m^2 (which is the estimated central intensity of the utilized lattice beams). Particles trapped in the periphery of the crystal experience much lower barriers and larger position spreads than particles trapped near the center. Since most particles are located in the peripheral shells of the crystals, the observed Bragg intensities

are lower and the Debye-Waller factors smaller than the central barrier heights might suggest.

B. PS- and SP- polarization

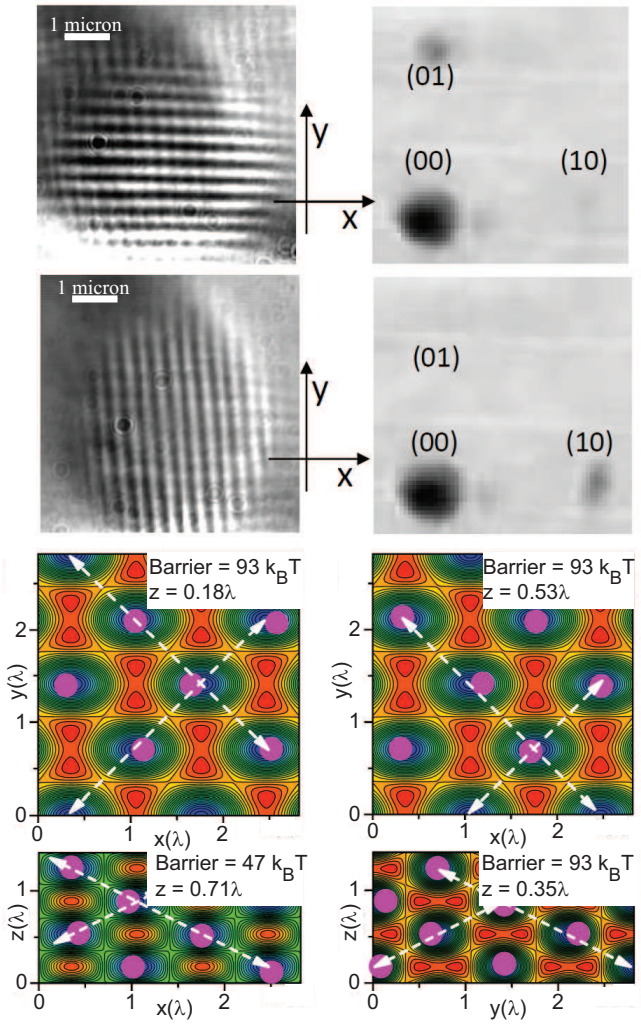

FIG. 5. Like Fig. 4 but for *sp* (top row) and *ps* (second row) polarizations. The color scale for the potential cuts ranges from -120k_BT (blue) to 0 (red) in steps of 5k_BT. The potential plots are for the case that the fields have no y-component (like the top row experimental data). (Color online.)

In Fig. 5 we show data analogous to those in Fig. 4, but with *sp*- and *ps*-polarization (top and second from top, respectively). While the potential still produces an FCO lattice structure as in the *pp*-polarization case, the potential barriers for particle migration in the x and y-directions differ by about a factor of two (see potential plots in Fig. 5). As a result, the particle x- and y-localizations are quite different. The crystal images clearly show that the particles are primarily localized in either x or y, but not both. Consequently, if the (10) Bragg peak is strong then the (01) peak is very weak, and vice versa. The direction of easy particle travel is along the projection of the laser beam polarizations into the $x-y$ plane. For instance, if the lattice beams have no y electric-field component, the direction of easy travel and large particle spread is the x-direction (top row and potential plots in Fig. 5). In both experimental situations shown in Fig. 5, the (11) signal is almost too weak to be observed. As in the *pp*-polarization case (Sec. VI A), this is because the Debye-Waller factor for the (11) peak is the product of the Debye-Waller factors for the (01) and (10) peaks (for homogeneous crystals).

C. SS- polarization

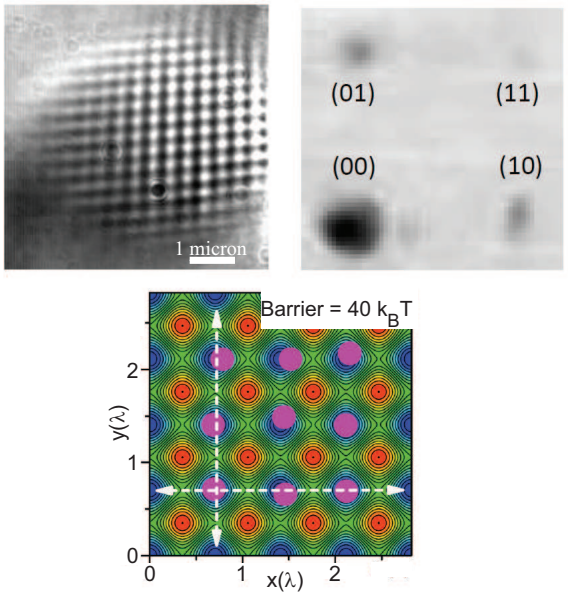

FIG. 6. Like Fig. 4 but for *ss*-polarization. The color scale for the potential cuts ranges from -85k_BT (blue) to 0 (red) in steps of 5k_BT. (Color online.)

In Fig. 6 we show data analogous to those in Figs. 4 and 5 for the case of *ss*-polarization. In this case, the light-induced potential does not depend on z, and is square and symmetric under x-y swap. While there is no periodic optical trapping force along z, particles are still attracted to the confocal point in the z-direction due to the overall weak gradient force caused by the intensity envelope of the lattice beams. The *ss*-configuration has the strongest x- and y-trapping forces of all the polarization cases. As a result, the crystal images generally suggest better particle localization in the *ss*-case than in all other cases, and the Bragg scattering peaks are generally stronger, with even the otherwise very faint (11) peak being visible in Fig. 6.

D. Crystal structure along z

In the present experimental setup, Bragg scattering involving $\Delta k_z \neq 0$ cannot be studied due to experimental constraints. However, three-dimensional ordering and stability of optically induced crystals was demonstrated previously based on the response of the optical crystals to certain manipulations. In Figure 4 of Ref. [18] we employed phase shifts of the lattice beams to translate an optical crystal back and forth along the z-direction, through the image plane. Snapshots extracted from the concurrently recorded movie showed recurring particle patterns, suggesting long-lived 3D ordering that persists throughout the phase manipulation sequence. For the large crystals we study in the present work, we infer 3D ordering and stability from recurring particle patterns on the *surface* of the crystal, observed while scanning the imaging plane or the crystal repeatedly back and forth along the z-direction. Further, watching the crystals in steady state, we observe well-defined surface details that show particles being trapped for long times in certain surface sites that are apparently preferred due to deviations of the optical-lattice beams from perfect symmetry. If there were no trapping in z-direction, the surface particles would rapidly diffuse in and out of the imaging focal plane. This is not observed; surface particles usually remain in focus for long times (seconds).

For the cases of *pp*-, *sp*- and *ps*-polarization, the existence of crystal structure in z is expected due to the periodic z-dependence of the optical trapping potential (see Figs. 4 and 5). Unexpectedly, we also find that the crystals with *ss*-polarization appear to be ordered along the z-direction, despite the *ss* optical trapping potential having no periodic dependence in z [18].

While our initial evidence of 3D crystals in the case of *ss*-polarization needs to be confirmed by Bragg scattering with $\Delta k_z \neq 0$, one may note that there have been earlier observations of particle ordering due to dipole interactions among particles [6]. In the present case of *ss*-polarization, it is possible that the optical potential imposes a crystal structure in x and y, while particle interactions lead to a well-defined structure in z. It may also be possible that the *ss*-configuration's periodic polarization gradient along the z-direction plays a role. Future Bragg scattering studies will help illuminate this issue. For details on the polarization gradient in the *ss*-polarized optical lattice, see Ref. [23] (Fig. 1(e) and associated discussion) and Ref. [31].

VII. CRYSTAL DISSIPATION

Optically induced crystals in aqueous solution are subject to the competing influences of the periodic optical lattice potential and Brownian motion. The lattice-induced optical dipole forces together with Stokes damping within the solvent (water) tend to localize the particles on a regular grid. The stochastic Brownian motion counteracts the formation and the maintenance of a crystal structure. In steady state, the crystal size grows until the outermost occupied lattice sites are only several k_BT deep. Bragg scattering is an excellent tool to study the buildup of the crystals, as well as their decay after the lattice is turned off.

We begin by discussing crystal decay. These studies are performed with 250 nm diameter particles, which have a 5% volume filling fraction in the FCO lattice structure shown in Fig. 2(a). For the measurements, the light-induced crystal is first allowed to reach steady state, which takes several minutes. Then, the lattice light is turned off for 25 ms and back on. The off phase is sufficiently long for the short-range crystal order to completely disappear, but not long enough for the particles to leave the vicinity of the trapping region. Upon turning the lattice back on the particles quickly become retrapped, and the crystal returns to its steady state within a few tens of milliseconds. This allows measurements to be repeated at a fairly high rate. In the present experiment, we use repetition rates of 1 to 2 per second. To measure the decay of the crystal order, an amplified photodiode is placed in the path of one of the Bragg reflections. The photodiode signal is proportional to the total power in the selected Bragg reflection. The decay of the photodiode signal after switching the lattice off is recorded with an oscilloscope and averaged over 128 cycles. The measurement is performed for several lattice laser powers and polarization configurations.

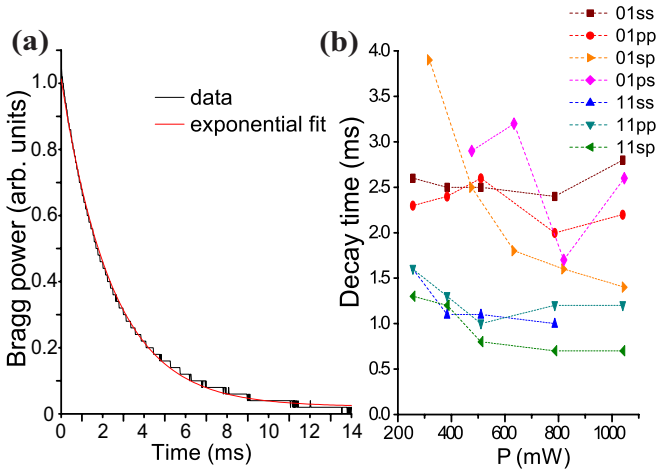

FIG. 7. (a) Example of an intensity decay curve for Bragg peak (10) at 480 mW total lattice power, 250 nm particles, and *sp*-polarization. (b) Decay time constants vs the total power of the lattice for the indicated polarization cases and Bragg peaks. (Color online.)

Generally, the decay curves are well fitted by decaying exponential curves, as shown by the example provided in Fig. 7(a). Plotting a set of decay time constants vs the laser power, we find that all (10) and (01) peaks have similar decay times that average to about 2.2 ms. The spread of the results comes from some uncertainty

in the fitting, which is due to 60 Hz and other noise in the photodiode signal. Notably, while the absolute Bragg reflection powers depend on the polarization type of the lattice, the decay times do not. For the (11) peaks we find decay times of about 1.1 ms, again with no dependence on the polarization type of the lattice. For both the (10)/(01) peaks and the (11) peaks we observe a drop in decay times with increasing laser power.

To explain the data in Fig. 7, we consider the square of the particle localization along the x-direction,

$$\begin{aligned}\langle x(t)^2\rangle &= \langle (x_0+\delta x(t))^2\rangle \\ &= \langle x_0^2\rangle + 2\langle x_0\delta x(t)\rangle + \langle \delta x(t)^2\rangle \\ &= \langle x_0^2\rangle + \langle \delta x(t)^2\rangle \end{aligned} \quad (5)$$

There, $\langle\rangle$ denotes an ensemble average, x_0 is the initial particle deviation when the lattice is turned off, and $\delta x(t)$ is the particle diffusion in position after the lattice is turned off. From the second to the third line we use the statistical independence of initial particle positions and subsequent drifts. Analogous equations apply to the y and z coordinates. In the case of crystal dissipation, the particles undergo Brownian motion with no external field, and therefore:

$$\langle x(t)^2\rangle = \langle x_0^2\rangle + \frac{2k_BT}{\gamma}t = \langle x_0^2\rangle + \frac{2k_BT}{6r\pi\eta}t \quad (6)$$

where T is the temperature, γ is the Stokes friction constant (friction force on sphere divided by velocity), r is the particle radius, and η is the water viscosity. Since the term $\langle x_0^2\rangle$ only depends on initial conditions, the decay behavior of the Debye-Waller factor depends only on the second term:

$$D_{10}(t) = D_{10}(0)\exp(-t/\tau_{10}) \quad (7)$$

where $D_{10}(0)$ is the Debye-Waller factor at the time instant of the lattice turn-off. Thus, the time constant

$$\tau_{10} = \frac{3r\eta\lambda^2}{8\pi k_BT} \quad , \quad (8)$$

where λ is the wavelength of the lattice light in the water-particle mix. Also, because of Eq. 2,

$$\tau_{10} = \tau_{10} \quad \text{and} \quad \tau_{11} = \tau_{01}/2 \quad . \quad (9)$$

To obtain λ we use an effective refractive index of the water-particle mix, $n_{\rm eff}$, which is the volume-weighted average of the refractive indices of water ($n_{\rm w} = 1.33$) and of polystyrene ($n_{\rm p} = 1.59$). The particle volume filling fractions, calculated in Ref. [18], are 2% for the 190 nm-diameter and 4.5% for the 250 nm-diameter particles. Consequently, $n_{\rm eff}$ is only slightly higher than $n_{\rm w}$; we use $n_{\rm eff} = 1.35$ for the 250 nm-diameter particles. The small difference between $n_{\rm eff}$ and $n_{\rm w}$ is not expected to have any observable effect. Using the water viscosity at 20°C, $\eta = 1.00\times10^{-3}$ Pa s, and the particle radius 125 nm, the decay times that follow from Eqs. 8f are $\tau_{10} = 2.33$ ms and $\tau_{11} = 1.17$ ms. These results are in excellent agreement with the experiment. The experimentally observed drop of the decay times at higher laser powers is consistent with a water temperature increase by about 10°C, which would reduce η by about 20%. This temperature increase with increased laser power is highly plausible.

The above analysis implies that, in agreement with the experiment, the decay time constants only depend on the lattice structure but not on the initial average position spread of the particles. Further, the Bragg-reflected field is a coherent sum of the scattered fields from individual particles (see Eq. 13 below). In the summation, correlations between initial particle deviations x_0 and absolute particle positions within the crystal are irrelevant. Hence, we do not expect any dependence of the decay behavior on systematic variations of $\langle x_0^2\rangle$ between particle sub-ensembles (such as the low-intensity outer regions of a crystal having a larger $\langle x_0^2\rangle$ than its high-intensity inner region). In our measurements we did not find evidence for any such dependence.

VIII. CRYSTAL RE-FORMATION

To study crystal formation from dense, disordered samples, we first allow the crystal to reach steady state (this takes several minutes). Then, the lattice light is turned off for sufficiently long that the short-range crystal order completely disappears, but not long enough for the particles to leave the trapping region, as described in Sec. VII. As the lattice is off for only 25 ms, during the lattice-off phase the particles on average move less than 300 nm due to diffusion, thus all remaining close to the wells from which they originate. Upon turning the lattice back on, the particles re-establish their steady-state localization within the lattice sites on a time scale that is on the order of 10 ms (which is four to five orders of magnitude faster than the time it takes to build an optical crystal "from scratch"). The process of re-establishing the short-range order is governed by both the lattice-induced optical dipole force and the stochastic force that causes Brownian motion. To investigate the re-formation of crystalline order, we measure the total power in a selected Bragg reflection vs time after switching the lattice on. As in Sec. VII, the experiment operates at repetition rates between 1 and 2 per second and we average over 128 cycles.

In Fig. 8(a) we show several typical rise curves at three different powers. Clearly, the rise curves are not simply exponential functions of time. It typically takes on the order of 1 ms for the Bragg reflectivity to begin building up. Then, for a few milliseconds the buildup of Bragg-reflected power appears quadratic in time. After tens of milliseconds the Bragg signals have a tendency to somewhat level out. However, in almost all cases we still observe noticeable upward slopes at the end of the observation time interval (23ms).

The crystal formation is considerably more compli-

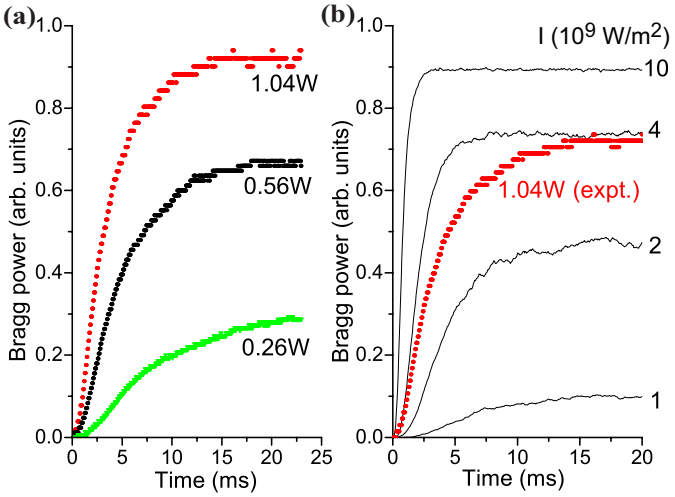

FIG. 8. (a) Bragg power vs time for the (10) Bragg peak at the three indicated total lattice laser powers, 250 nm particles, *pp*-polarization, and $\phi \approx 45°$. The lattice is turned on at time $t = 0$. (b) Rise curves simulated using the Langevin equation for the (10) Bragg peak at the indicated fixed single-beam lattice intensities, *pp*-polarization and $\phi = 45°$. The simulated curves are normalized as explained after Eq. 13. (Color online.)

cated than the decay studied in Sec. VII. In the case of crystal decay, the particle delocalization behavior simply follow $\langle \delta x(t)^2 \rangle = 2Ft$, with the diffusion constant $F = k_B T/\gamma$, regardless of the initial particle positions within the overall crystal. In the case of crystal formation, the particle dynamics depend on both the light-induced forces, which strongly depend on particle position within the overall crystal, and on the stochastic forces, whose characteristics do not depend on particle position. As a result, the rise behavior is strongly affected by the Gaussian intensity envelopes of the lattice beams, as we will show next.

In order to understand data like the ones shown in Fig. 8(a), we simulate the particle dynamics after lattice turn-on, employing the Langevin equation using methods described by Risken [21]. (An alternate, but more computationally-intensive, method would be to use the Fokker-Planck equation.) The Langevin equation, describing the motion of a particle in a fluid, is

$$m\ddot{\mathbf{x}} = -\nabla V(\mathbf{x}) - \gamma\dot{\mathbf{x}} + \mathbf{\Gamma}(t) \qquad (10)$$

where $\mathbf{x}(t)$ is the particle position, m the particle mass, and $\mathbf{\Gamma}(t)$ a δ-correlated stochastic force with $\langle \mathbf{\Gamma} \rangle = 0$ and $\langle \mathbf{\Gamma}_i(t)\mathbf{\Gamma}_j(t') \rangle = 2k_B T\gamma\delta_{ij}\delta(t-t')$. $V(\mathbf{x})$ is the particle trapping potential, which depends on polarizations, intensity and ϕ (equations given in Ref. [18]). We use Eq. 10 to compute ensembles of particle trajectories:

$$\begin{aligned} \mathbf{v}(t+\Delta t) &= \mathbf{v}(t)(1-\gamma\Delta t/m) - [\nabla V(\mathbf{x})/m]\,\Delta t \\ &\quad + \sqrt{2\gamma k_B T \Delta t/m^2}\,\mathbf{w} \\ \mathbf{x}(t+\Delta t) &= \mathbf{x}(t) + \mathbf{v}(t)\Delta t \end{aligned} \qquad (11)$$

There, $\mathbf{v}(t)$ is the velocity vector of a particle. The time step size Δt is chosen to be 1 ns, which is much less than the velocity correlation time (which is about 6 ns). The spatial vector $\mathbf{w}$ contains three random numbers w_i for the random velocity increments in the x, y and z degrees of freedom, respectively. The w_i follow a Gaussian distribution and have an RMS value of one. The w_i can be generated via [21]

$$w_i = \sqrt{\frac{12}{M}} \sum_{n=1}^{M} (r_n - \frac{1}{2}) \qquad (12)$$

with $M \sim 10$ and random numbers r_n that have a flat distribution between 0 and 1. Once the particle trajectories $\mathbf{x}_n(t)$ are known, the Bragg scattering amplitudes are proportional to

$$A(t, \Delta\mathbf{k}) = \frac{1}{N} \sum_{n=1}^{N} \exp(-\mathrm{i}\Delta\mathbf{k} \cdot \mathbf{x}_n(\mathrm{t})) \quad . \qquad (13)$$

There, $\Delta\mathbf{k}$ is the reciprocal lattice vector that corresponds to the Bragg peak. The Bragg scattering powers are $\propto A\,A^*$. Equation 13 is normalized such that a crystal has a Bragg scattering intensity of 1 if all particles have zero displacement.

In Fig. 8(b) we compare a selected experimental result with simulation results for optical lattices in which each of the four beams has the indicated single-beam intensities I. We find that the quadratic onset of the experimentally observed Bragg signal vs time is reproduced fairly well by the simulations in the range $2\times10^9 \mathrm{W/m^2} < I < 4\times10^9 \mathrm{W/m^2}$. However, this model cannot achieve agreement with the measured curve over the entire time range.

To improve the model, we find it is important to include the variation of the potential depth throughout the volume of the trapping region. Particles near the center, where the potential is deeper, localize fast and contribute quickly to the Bragg scattering amplitude. Particles farther out experience shallower potentials and localize more slowly, so their contribution to the Bragg scattering amplitude develops more slowly. We must also account for the geometric fact that the outer shells contain more lattice sites than the inner ones, so there are more particles in the low-intensity outer shells of the lattice than in the small high-intensity center. The Bragg amplitudes from all shells must be weighted and coherently summed before calculating the Bragg intensity.

To implement this improved model, we calculate and store the complex Bragg amplitudes generated by 5000 particles that are randomly released into lattices with well-defined single-beam intensities I. The procedure

is performed for a selection of I_i ranging from $0.25 \times 10^9 \mathrm{W/m^2}$ to $12 \times 10^9 \mathrm{W/m^2}$ in steps of $\Delta I = 0.25 \times 10^9 \mathrm{W/m^2}$. In this way an array of 48 complex Bragg amplitude curves is generated. To obtain a net Bragg amplitude, the intensity-specific Bragg amplitude curves are added up with weighting factors that are proportional to the number of particles we expect for the respective intensities in the inhomogeneous lattice potential. The magnitude of the weighted amplitude sum is then squared, resulting in Bragg intensity curves for the entire inhomogeneous lattice.

In choosing the weighting factors, we note that the confocal parameter of the lattice beams is quite large in comparison with the diameter of the crystals (~ 200 μm vs ~ 10 μm). Therefore, we use weighting factors for an intensity distribution that is Gaussian in the xy plane and does not depend on z (2D weighting). For a single-beam peak intensity $I_{\max}$, the weighting factor for intensity step $I_i < I_{\max}$ then is proportional to the area between circles with scaled radii $r_{+,i}$ and $r_{-,i}$ given by

$$r_{+,i} = \sqrt{\ln\left(\frac{I_{\max}}{I_i - \Delta I/2}\right)} \quad r_{-,i} = \sqrt{\ln\left(\frac{I_{\max}}{I_i + \Delta I/2}\right)}$$

The weighting factors increase with decreasing intensity, in accordance with there being more particles in the larger low-intensity perimeter of the beams than there are in the smaller peak-intensity central region. The weighting factors only depend on the assumed Gaussian beam shape, not on the overall diameter of the Gaussian.

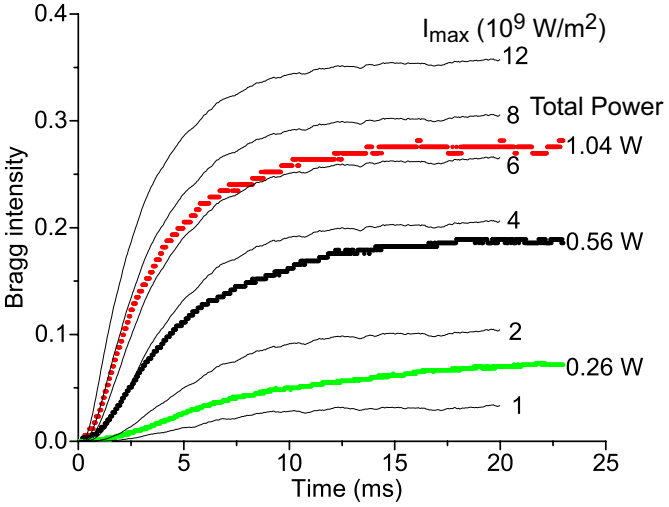

FIG. 9. Comparison between measured Bragg scattering rise curves at the three indicated total lattice laser powers ((10)-peak, 250 nm particles, *pp*-polarization, $\phi \approx 45°$) and corresponding simulated rise curves for Gaussian lattice intensity distributions with the indicated central intensities. The Bragg signals of the experimental curves are scaled to best match the simulations. The simulated curves are normalized as explained after Eq. 13. (Color online.)

We find the model to be quite successful in describing the rise of the Bragg-scattered power, as seen in Fig. 9. Considering the 60% transmission of the objectives and the estimated 5 μm full-width-at-half-maximum diameters of the lattice beams, the estimated single-beam peak intensities for the three experimental cases shown in Fig. 9 are 5.5×10^9 W/m^2, 2.9×10^9 W/m^2, and 1.4×10^9 W/m^2. These values are in good qualitative agreement with the central intensities of the simulated curves that fit the experimental curves best. Similar levels of agreement are obtained for other Bragg peaks and other polarization cases. In view of the success of the model, we conclude that the gradual increase in Bragg signal at later times is indeed due to the delayed buildup of the Bragg signal from the outer, low-intensity layers of the crystal.

IX. DISCUSSION

We have created optically-induced crystals of thousands of sub-micron particles in aqueous solution using a four-beam optical lattice (air wavelength 1064 nm) with several polarization and angle degrees of freedom. Using microscopic images and Bragg scattering patterns obtained with a 532 nm probe beam, we have analyzed the crystals and observed agreement with expectations from calculated single-particle optical trapping potentials. An indication of particle-particle interaction has been found in the *ss*-polarization configuration, where crystals appear to be ordered in all three degrees of freedom while the optical single-particle potential only depends on x and y. Future Bragg scattering work is planned to follow up on this.

The dependence of Bragg scattering on particle localization in a lattice has lead us to a novel method of studying Brownian motion in external trapping potentials. The time dependence of the Bragg scattering power, observed upon switching the lattice on and off, has been explained by a quantitative model. A critical component necessary to explain the lattice growth behavior is to account for the intricate interplay between Brownian motion and particle localization in the inhomogeneous lattice potential, which we have simulated using the Langevin equation. The analysis shows that there are copious numbers of particles trapped in the peripheral regions of the approximately Gaussian optical-lattice beams. The measured Bragg reflectivities are therefore dominated by the particle behavior in the periphery of the crystals, where the trapping potentials are shallow, the particle localization buildup is slow, and the ultimate RMS position spread of the particles is quite large (about 100 nm at 1×10^9 W/m^2). This finding is relevant to potential future applications of optically-induced crystals.

The results presented in this work suggest strategies for how to achieve better particle localization. We are currently investigating a scheme in which particles are trapped exclusively within the central, high-intensity region of an optical lattice. In this scheme, a pulsed increase of the lattice power for $\lesssim 1$ ms would lead to a

rapid improvement of the localization of all particles at their lattice sites. The pulse is sufficiently short that no additional particles would be accumulated in the lattice fringe fields. Due to the short pulse duration, the intensity enhancement factor can be chosen to be very large without risk of overheating the sample. The particle localization at 3×10^11 W/m^2 is expected to be 5 nm, which would be sufficiently small for high-resolution Bragg structure analysis of the trapped particles. This degree of localization would be ideal for extensions of the work towards crystallography of non-spherical trapped objects, such as large biological molecules, in the spectral region of the water window (Bragg probe wavelength 2.34 nm to 4.4 nm).

The success of our theoretical model suggests that we can properly describe the Brownian motion in the lattice, that our model properly accounts for lattice inhomogeneity effects, and that particle interactions do not significantly alter the particle dynamics. For the utilized particle size and lattice geometry, only one particle can fit within each lattice well. Using smaller particles, it would in principle become possible to have more than one particle within a lattice well. In this case, particle interactions due to electric charges on the particles, as well as electric-dipole forces between them, are expected to become more important. With larger particles, the particles would fill a larger fraction of the volume and would interact more strongly with each other, due to collisions and electrostatic forces, as well as with the lattice light field. Higher-resolution Bragg scattering would enable the investigation of such richer systems.

ACKNOWLEDGMENTS

We would like to thank Professor Chris Meiners for letting us use his lab to prepare samples. This work was supported by NSF Grants No. PHY-0855871 and No. PHY-0114336.

[1] A. Ashkin, Phys. Rev. Lett. **24**, 156 (1970).
[2] A. Ashkin, Science **210**, 1081 (1980).
[3] A. Ashkin, J. M. Dziedzic, J. E. Bjorkholm, and S. Chu, Opt. Lett. **11**, 288 (1986).
[4] A. Jonáš and P. Zemánek, Electrophoresis **29**, 4813 (2008).
[5] M. Lang and S. Block, Am. J. Phys. **71**, 201 (2003).
[6] M. M. Burns, J. M. Fournier, and J. A. Golovchenko, Science **249**, 749 (1990).
[7] A. E. Chiou, W. Wang, G. J. Sonek, J. Hong, and M. W. Berns, Opt. Comm. **133**, 7 (1997).
[8] M. P. MacDonald, L. Paterson, K. Volke-Sepulveda, J. Arlt, W. Sibbett, and K. Dholakia, Science **296**, 1101 (2002).
[9] A. N. Rubinov, V. M. Katarkevich, A. A. Afanas'ev, , and T. S. Efendiev, Opt. Comm. **224**, 97 (2003).
[10] A. Casaburi, G. Pesce, P. Zemanek, and A. Sasso, Opt. Comm. **251**, 393 (2005).
[11] M. Reicherter, T. Haist, E. U. Wagemann, and H. J. Tiziani, Opt. Lett. **24**, 608 (1999).
[12] D. G. Grier, Nature **424**, 21 (2003).
[13] J. Leach, G. Sinclair, P. Jordan, J. Courtial, M. Padgett, J. Cooper, and Z. Laczik, Opt. Exp. **12**, 220 (2004).
[14] H. Melville, G. Milne, G. Spalding, W. Sibbett, K. Dholakia, and D. McGloin, Opt. Exp. **11**, 3562 (2003).
[15] P. J. Rodrigo, V. R. Daria, and J. Gluckstad, Opt. Lett. **29**, 2270 (2004).
[16] P. Zemánek, A. Jonáš, L. Šrámek, and M. Liška, Opt. Lett. **24**, 1448 (1999).
[17] J.-M. Fournier, J. Rohner, P. Jacquot, R. Johann, S. Mias, and R.-P. Salath, Proc. SPIE - Int. Soc. Opt. Eng. **5930**, 59300Y (2005).
[18] B. N. Slama-Eliau and G. Raithel, Phys. Rev. E **83**, 051406 (2011).
[19] P. S. Jessen and I. H. Deutsch, Adv. Atom. Mol. Opt. Phy. **37**, 95 (1996).
[20] N. V. Morrow and G. Raithel, Adv. Atom. Mol. Opt. Phy. **53**, 187 (2006).
[21] H. Risken, *The Fokker-Planck Equation: Methods of Solutions and Applications* (Springer, Berlin, 1989).
[22] G. Grynberg, B. Lounis, P. Verkerk, J.-Y. Courtois, and C. Salomon, Phys. Rev. Lett. **70**, 2249 (1993).
[23] K. I. Petsas, A. B. Coates, and G. Grynberg, Phys. Rev. A **50**, 5173 (1994).
[24] G. Birkl, M. Gatzke, I. H. Deutsch, S. L. Rolston, and W. D. Phillips, Phys. Rev. Lett. **75**, 2823 (1995).
[25] A. Gorlitz, M. Weidemuller, T. W. Hansch, and A. Hemmerich, Phys. Rev. Lett. **78**, 2096 (1997).
[26] G. Raithel, G. Birkl, A. Kastberg, W. D. Phillips, and S. L. Rolston, Phys. Rev. Lett **78**, 630 (1997).
[27] G. Raithel, G. Birkl, W. D. Phillips, and S. L. Rolston, Phys. Rev. Lett. **78**, 2928 (1997).
[28] G. Grynberg and C. Robilliard, Phys. Rep. **355**, 335 (2001).
[29] I. H. Deutsch, R. J. C. Spreeuw, S. L. Rolston, and W. D. Phillips, Phys. Rev. A **52**, 1394 (1995).
[30] K. C. Neuman and S. M. Block, Rev. Sci. Instr. **75**, 2787 (2004).
[31] A. Kastberg, W. D. Phillips, S. L. Rolston, R. J. C. Spreeuw, and P. S. Jessen, Phys. Rev. Lett. **74**, 1542 (1995).
[32] H. J. Metcalf and P. V. der Straten, *Laser cooling and trapping* (Springer, New York, 1999).